Welding in the World (2021) 65:329–343
https://doi.org/10.1007/s40194-020-01014-x

RESEARCH PAPER

Evolution of microstructure and mechanical properties on dissimilar transient liquid phase (TLP) bonding of GTD-111 and IN-718 by BNi-9 (AWS A5.8/A5.8M) interlayer

Ali Izadi Ghahferokhi[1] · Masoud Kasiri-Asgarani[1] · Kamran Amini[2] · Reza Ebrahimi-kahrizsangi[1] · Mahdi Rafiei[1]

Received: 11 March 2020 / Accepted: 12 October 2020 / Published online: 31 October 2020

Abstract
Dissimilar transient liquid phase (TLP) bonding of GTD-111 and IN-718 nickel-based superalloys was investigated using BNi-9 (AWS A5.8/A5.8M) as an interlayer. The effect of the bonding time on the microstructure and mechanical properties of the TLP-bonded specimens was studied at 1100 °C using optical microscopy (OM), scanning electron microscopy (SEM) equipped with energy-dispersive spectrometry (EDS), and micro-hardness and shear strength analyses. Joint microstructural studies revealed that at the bonding times shorter than 75 min, nickel- and chromium-rich borides were formed with the joint centerline. The volume fraction of intermetallic compounds decreased with the increase of the bonding time and the diffusion of boron element whereby the isothermal solidification eventually completed after 75 min. Micro-hardness investigations along the bonding joint showed that the hardness of an isothermal solidification zone (ISZ) decreased with the completion of isothermal solidification. The hardest zone in the joint structure belonged to the athermal solidification zone (ASZ). The shear strength test results showed that incrementing the bonding time increased the shear strength where the shear strength value at 1 min/1100 °C (320 MPa) raised to 590 MPa after the completion of isothermal solidification.

Keywords TLP bonding · GTD-111 superalloy · IN718 superalloy · BNi-9 interlayer · Mechanical properties · Bonding time

1 Introduction

Nickel-based superalloys have multiple interesting specifications such as outstanding high-temperature tensile strength and microstructural stability, good fatigue strength, and satisfactory creep and stress rupture properties along with proper oxidation and corrosion resistance [1]. These specifications make superalloys a good option for manufacturing the components used in gas turbines due to their complex shape configurations [2], albeit it is inevitable to confront defects such as formation of thermal fatigue and corrosion cracks at high operational temperatures. Repairing processes such as joining methods are used to restore damaged parts to an applicable condition [3]. Common joining processes carried out in industry include diffusion bonding, brazing, and fusion welding [4]. High pressure requirement during diffusion bonding and brittle phase formation could severely affect the mechanical integrity of joints in the brazing process [5–7]. Additionally, hot cracks in both seams and hot affected zone fusion (HAZ) during fusion welding are some of the unavoidable restricting defects in the aforementioned techniques [8, 9].

Based on the studies conducted by several researchers, during conventional fusion welding processes, liquation crack occurs in the HAZ and solidification cracking occurs in the seam zone. The main weldability concern in repairing nickel-based superalloys is the HAZ liquation cracking. The combined effects of boron carbide constitutional liquation, δ phase dissolution–promoted liquation, and grain boundary

This article is part of the Topical Collection on Recommended for publication by Commission XVII - Brazing, Soldering and Diffusion Bonding

✉ Masoud Kasiri-Asgarani
m.kasiri.a@gmail.com; m.kasiri@pmt.iaun.ac.ir

✉ Kamran Amini
kamran_amini1978@hotmail.com

[1] Advanced Materials Research Center, Department of Materials Engineering, Najafabad Branch, Islamic Azad University, Najafabad, Iran

[2] Center for Advanced Engineering Research, Majlesi Branch, Islamic Azad University, Isfahan, Iran

segregation are the main factors involved in increasing the susceptibility of 718 alloy to liquation cracking [10, 11]. Ahn et al. [12, 13] reported that the solidification cracking was nearly related to the carbides and Laves eutectic constituents formed along the grain boundaries.

Therefore, a combination of diffusion bonding and brazing techniques known as transient liquid phase (TLP) method is a preferable choice for the joining/repairing process using Ni-based superalloys [11, 14–16].

Bakhtiari et al. studied the mechanical properties of IN738/MBF20/IN718 dissimilar system based on the repair process of the related gas turbine parts [17].

The TLP bonding is a process in which a flimsy interlayer containing the melting point depressant (MPD) elements is placed between the two base metal parts [18]. The solid interlayer melts while heating the joining specimens to the bonding temperatures, where holding the assembly at the bonding temperatures causes the diffusion of the MPD elements into the solid base metal which results in isothermal solidification. After the completion of isothermal solidification, the joint becomes almost indiscernible from the base metals and the liquid phase totally vanished [19].

IN-718 is a precipitation hardening nickel–based superalloy which is used in manufacturing gas turbine engine components such as disks, shells, shafts, blades, stators, seals, supports, and tubes and in strengthening [20, 21]. Pouranvari et al. studied solid-state precipitation and solidification phenomena during the TLP bonding of IN718 nickel–based superalloy using BNi-3 (wt.%) ternary filler alloy. Broad Cr–Mo–Nb-rich boride precipitates were formed in the base metal region due to boron diffusion into the substrate during the bonding process. GTD-111 is another nickel-based superalloy which was employed in industrial applications in the 1980s. Compared to IN-738LC, GTD-111 has superb high-temperature properties, as a result of which the alloy substituted for the conventional IN-738LC in high-temperature gas turbines at higher temperatures. Refractory elements such as W, Cr, Ta, Co, and Mo in this alloy prevent local hot corrosion. It is also known that GTD-111 has 20 °C higher creep strength compared with IN-738LC [22, 23]. Amiri et al. evaluated the microstructure and mechanical properties of the TLP bonding of GTD-111superalloy using the MBF20 interlayer. They reported that throughout cooling the intermetallic compounds and eutectic or nickel-rich and chromium-rich borides, Ni–Si–B compound and eutectic-γ continuously formed in the bonding region. With the increase of time, thickness and continuity of the intermetallic phases decreased and the intermetallic phases eliminated due to the increasing bonding temperature of 1180 °C They showed that the shear strength of the joints increased with the increasing bonding time and homogenization of the specimens after the joining process resulted in a greater uniform hardness profile in the joint and also a notable increase in the shear strength up to 97% of the substrate strength. BNi-9 is a eutectic nickel-based brazing alloy that is appropriate for brazing nickel, superalloys, stainless steels, and other assemblies which require good joint strength at high temperatures with excellent corrosion and oxidation resistance. As indicated by Ohsasa et al. [24], the ternary Ni–Cr–B fillers with a composition similar to BNi-9 have been promoted as an alternative for industrial brazing since the addition of chromium leads to a higher corrosion resistance of the brazing joint and prevents oxidation. Regarding ternary alloys of BNi-9, Bondar [25] proposes the following solidification path at equilibrium: L ➔ primary α ➔ $\alpha + (Ni,Cr)_3B$ ➔ $\alpha + (Ni,Cr)_3B + CrB$. Recently, Siredey-Schwaller et al. [26] have scrutinized the six various brazing alloys containing Ni–Cr–Si–B with a similar boron content (3 wt.%). The first reaction of solidification sequence for all six alloys showed the formation of α Ni-solid solution, followed by the formation of a eutectic phase that is composed of the two phases of α and $(Ni,Cr)_3B$. Based on their results, the last reaction depends on the alloy. Solidification of the Cr-rich alloys such as BNi-9 ends with the reaction L ➔ $\alpha +$ $(Ni,Cr)_3B + CrB$, and solidification of the Si-rich alloys such as BNi-3 and other alloys is completed with the L ➔ $\alpha +$ $(Ni,(Cr))_3B + \beta_3$-Ni_3Si reaction.

In this study, BNi-9 filler metal was used as the interlayer for the TLP bonding of dissimilar GTD-111 and IN 718 superalloys, and the microstructure, the bonding behavior, and mechanical properties of the entire compound were investigated.

2 Experimental techniques

The compositions of GTD-111 and IN718 as the base metals and the BNi-9 interlayer are given in Table 1. The joining metal specimens were cut into dimensions of 10 mm×10 mm×5 mm using a wire cutting machine. The joining surfaces were grounded using the grit sizes of No. 60–1500 SiC emery sheets. The samples were cleaned for 15 min in an acetone ultrasonic bath followed by the TLP bonding process in a vacuum furnace with the applied bonding pressure of 10^{-2} Torr. Thickness of the amorphous foil used for the interlayer was 50 μm. The bonded samples were prepared metallographically (perpendicularly sectioned to the bond), and the sectioned specimens were ground using the grit sizes of No. 80–3000 SiC paper. After that, the specimens were polished by disc polishing using Al_2O_3 solution so as to achieve a mirror finish of 1 μm on the welds. After metallographic preparation, the specimens were studied using optical (OM) and scanning electron microscopies (SEM) equipped with energy-dispersive spectrometry (EDS). The bonding was developed at 1100 °C for 1, 15, 30, 45, 60, and 75 min. The heating rate was 15 °C/min, and the cooling was done in situ. Fixing of the samples and the interlayer by the fixture for the TLP bonding process is shown in Fig. 1.

Table 1 Composition in mass% of the base metal and interlayer

	Ni	Cr	Co	Ti	Al	W	Mo	Ta	Fe	Nb	C	B	Si
GTD-111	Ball	13.5	9.5	4.75	3.3	3.8	1.53	2.7	0.23	-	0.09	0.01	-
IN718	Ball	18	0.06	0.92	0.4	-	3.30	0.05	17.86	4.41	0.03	0.007	-
BNi-9	Ball	15	-	-	-	-	-	-	1.5	-	-	3.6	-

The specimens were etched in two different etchants in order to study their microstructural properties. In order to show the precipitates adjacent to the interlayer/base metal interface, Murakami etchant (10 g KOH, 10 g $K_3[Fe(CN)_6]$, and 100 mL H_2O) was used which favorably etches the Cr-rich phases. Moreover, the $\gamma-\gamma'$ microstructure of isothermally brazed joints was recognized by applying Kalling's reagent (1.5 g $CuCl_2$ + 33 mL ethanol + 33 mL H_2O + 33 mL HCl) which favorably etches the γ phase. Scanning electron microscopy was employed in order to investigate the microstructure of the bonding region, and energy-dispersive X-ray spectroscopy (EDS) was used to determine the chemical composition. Mechanical properties were investigated and evaluated by employing the shear strength and hardness test.

Primary microstructural studies of the joint were performed using an Olympus OM. Microstructural evaluation and semi-quantitative compositional analysis were performed employing a FEI-QUANTA FEG450 SEM equipped with ultra-thin window EDS.

The shear strength and micro-hardness test were chosen for the assessment of mechanical properties of the joint. For testing the shear strength a Zwick/Roell tensile machine was used with a cross-head speed of 1 $mm{\cdot}min^{-1}$ at room temperature. A shear test jig was designed to hold the samples from the D3 tool steel. Micro-hardness measurement across the bond area was carried out using a Buehler Micromet machine by Vickers micro-hardness test with a 20-g load.

3 Results and discussion

3.1 Microstructure of base metals

Figure 2 demonstrates the macrograph of the GTD-111 specimen obtained from scanning electron microscopy. The microstructure was composed of a γ solid solution as the matrix accompanied by finely dispersed γ' precipitates. During the solidification process, carbides and $\gamma-\gamma'$ eutectic islands were formed in the microstructure. Because of the precipitation of large γ' particles close to the grain boundaries as a result of irregular movement of the grain boundaries, the presence of serrated grain boundaries can be seen in the microstructure presented in Fig. 2 [27]. $(Cr,Mo)_{23}C_6$ and (Ta,W,Ti)C carbides that have a FCC crystal structure [28] are the most usual carbides which are formed during the solidification of the GTD-111 alloy.

Having a multiphase microstructure, GTD-111 alloy contains the γ matrix, bimodal γ' precipitates, $\gamma-\gamma'$ eutectics, carbides, and a small amount of inappropriate phases such asδ,η, σ, and Laves. The γ' super-lattice phase which has the $L1_2$-type structure is mainly made of Ni_3(Al, Ti). Throughout the solidification process at 1200 °C, primary γ' semi-cubes with the 0.8-μm edge dimension are produced. Following that, during aging after partial solution treatment, the secondary γ' semi-spheres with 0.1 μm diameter emerged [3]. Some technical data for GTD-111 were reported by Daleo and Wilson [29]. The GTD-111 alloy is a modification of IN738LC. By applying a chemical extraction method, the total

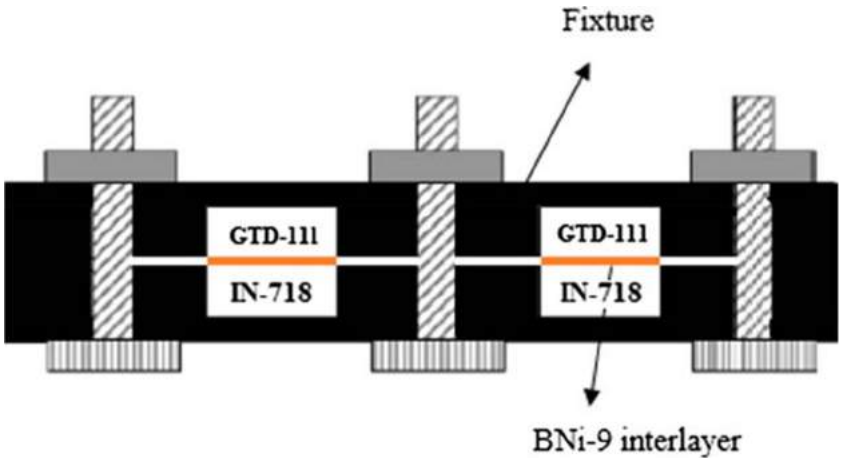

Fig. 1 Schematic illustration of fixture for TLP bonding process

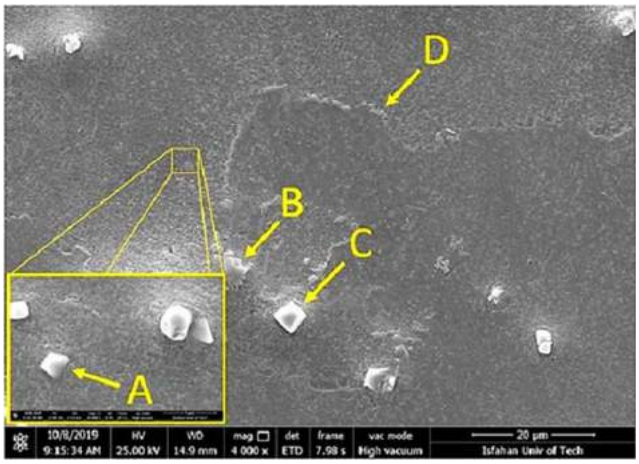

Fig. 2 SEM image of the GTD-111 base metal. **a** γ' particles (precipitates). **b** $\gamma-\gamma'$ eutectic areas. **c** Carbides (white lumpy shape). **d** Serrated grain boundaries

γ' volume fraction of GTD-111 was determined to be above 60%, which is 15–20% more than the corresponding value (45%) for IN738LC.

Also, carbides are visible in the grain boundaries which are uniformly distributed within the grains. Based on the chemical analyses, the MC-type carbides (where M = Ti, W, and Ta) are identified as the main carbide types formed within the grains, while the $M_{23}C_6$-type carbides are visible at the grain boundaries (where M stands for Mo and Cr). Further chemical analyses spotted oxide, nitride, or carbo-nitride particles formed as white spots inside random carbides. The $\gamma-\gamma'$ eutectics emerged throughout the last stages of solidification. This can be verified by the fact that these eutectics are often scattered near micropores at dendrite boundaries [30].

The SEM micrograph of the IN-718 specimen is shown in Fig. 3. As observed and verified by EDS analysis, a number of titanium and niobium carbide particles are randomly distributed. Due to the existence of carbon content beyond 0.02 wt.% in the IN-718 alloy, finely distributed carbides are formed in the structure, as shown in Fig. 3. The original content of Nb in IN718 is about 3 wt.%. The amount of Nb in IN718 leads to the precipitation of gamma double prime (γ''). The microstructure of IN718 contains a nickel-rich austenitic solid solution γ phase matrix, carbides, flower-like $\gamma-\gamma'$-phase eutectic islands, and very fine cubic/spherical γ'-phase particles with $Ni_3(Nb,Ti)$ formulation. MC, $M_{23}C_6$, and M_6C are the general carbides.

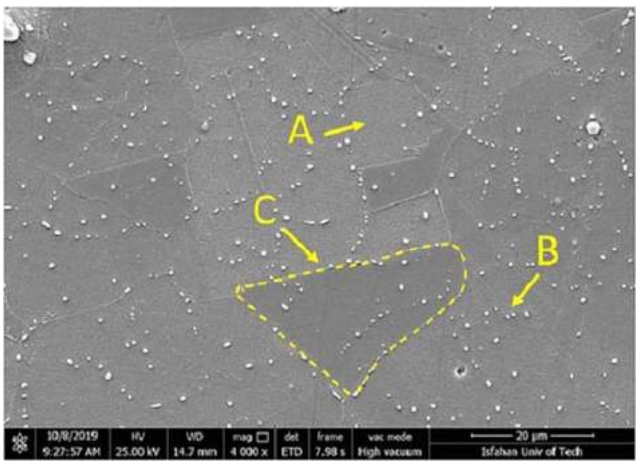

Fig. 3 SEM image of the 718 base metal. **a** γ' particles (precipitates). **b** Carbide particles of titanium and niobium. **c** Gamma double prime (γ'') microstructure

3.2 Microstructure of the joint

The OM image of a typical microstructure of GTD111/BNi-9/IN718 bonded at 1100 °C/60 min is shown in Fig. 4. The distinct zones which are visible in this image are defined as follows:

(i) IN-718 base metal
(ii) IN-718 side diffusion affected zone (DAZ-IN-718)
(iii) Isothermal solidification zone (ISZ)
(iv) Athermal solidification zone (ASZ)
(v) GTD-111 side diffusion affected zone (DAZ-GTD-111)
(vi) GTD-111 base metal

From these 6 distinct zones, 3 zones are related to the joint area that will be described below.

3.3 Isothermal solidification zone

The main reason for the melts of the interlayer and important interdiffusion between the interlayer and the base metal is the lower melting point of the interlayer than the bonding temperature. Diffusion of MPD elements from the molten interlayer into the base metal is the first compositional change in the liquid phase and raises its temperature. The solidification phenomenon involves two modes: mode I is the isothermal solidification and mode II is the athermal solidification. Isothermal solidification starts with the reach of the liquidus temperature to the bonding temperature (T_B). The interlayer melting

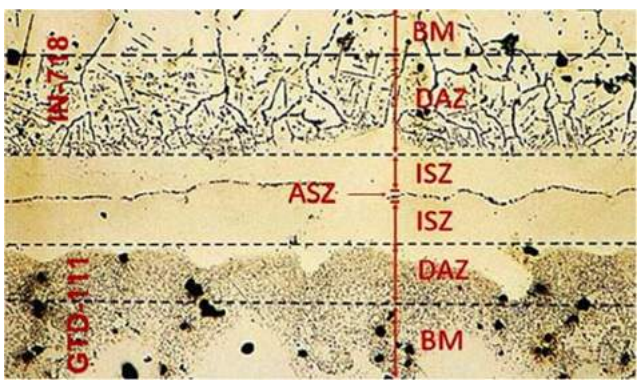

Fig. 4 Optical microscopy image of the GTD111/BNi-9/I N718 system at 1100 °C/60 min

temperature is 1055 °C [31] which is lower than the bonding temperature (1100 °C). Therefore, the interlayer melting is assured at 1100 °C. The chemical compositional changes of the liquid phase swirl the liquidus temperature. The main indicator for the alloying element effect on the liquidus temperature is the distribution coefficient (k) [32]. For increasing the liquidus temperature of the liquid phase, two phenomena are helpful:

(A) Emptying of the liquid phase from elements with k value less than unity such as the MPD elements causes the raising of the liquidus temperature of the liquid phase.
(B) The presence of elements with the k value larger than unity such as Cr and Fe in the liquid shows the dissolution of the base metal and Cr and Fe diffusion from the base metal into the bond area during the bonding process which will cause the raising of the liquidus temperature of the liquid phase. With adequate bonding time, the isothermal solidification was achieved at a constant temperature. Figure 4 shows the microstructure of GTD-111/BNi-9/IN 718 system at 1100 °C/45 min. The bonding area consists of ASZ adjacent to two ISZs. The EDS analysis of ISZ is given in Table 2.

In the lack of temperature reduction, the rejection of solute elements at the solid/liquid interface is not permitted. This is the reason for the disappearance of second phase in the ISZ. There are no elements of Cr, Al, Co, Ti, Nb, and Si in the interlayer, but their presence shows the base metal dissolution. The existence of these elements results in an increment in the liquidus temperature until reaching the bonding temperature at which isothermal solidification is commenced. Based on the solidification sequences, one can investigate the diffusion of MPD elements such as B and Si from the bonding zone into the base metal and vice versa which is the most prominent cause for the compositional changes of the melt phase. In the joint centerline, the ISZ can be observed that is a merely narrow zone consisting of the proeutectic γ solid solution (this is the zone at which there is no sign of any eutectic phases or even precipitated γ').

Table 2 EDS analysis of the ISZ

Element	Weight %	Atomic %	Weight %	Atomic %
	ISZ in side of IN-718		ISZ in side of GTD-111	
$Al_{(K)}$	0.07	0.16	0.39	0.86
$Si_{(K)}$	1.68	3.54	0.98	2.07
$Nb_{(L)}$	4.43	2.82	4.14	2.65
$Ti_{(K)}$	2.08	2.57	1.75	2.16
$Cr_{(K)}$	11.24	12.77	12.12	13.82
$Fe_{(K)}$	4.50	4.76	5.09	5.40
$Co_{(K)}$	2.58	2.59	2.80	2.81
$Ni_{(K)}$	68.81	69.29	68.02	68.69
$Ta_{(L)}$	2.81	0.92	2.52	0.83
$W_{(L)}$	1.80	0.58	2.19	0.70

3.4 Athermal solidification zone

The ASZ contains a eutectic structure of various zones of the specimen microstructure. This zone is produced because of insufficient bonding time and failure of isothermal solidification of the remaining liquid phase in the centerline. Its solidification during the cooling cycle in the case of insufficient bonding time can lead to the formation of the ASZ. The EDS analysis of the ASZ is shown in Fig. 5.

The Ni-rich borides of eutectic Ni_3B are illustrated as a eutectic shape and the Cr-rich borides of CrB are indicated as the dark phase. The aforementioned interlayer is a Ni-based one in which the MPD element is boron. Due to insufficient time for the complete diffusion of solute atom (B) into the base metal, this element was segregated to the residual melt, which resulted in the formation of the ASZ. Figure 6 shows the microstructure of the ASZ in the bond region for 60 min. The microstructure of the ASZ in the joint with the existence of a high content of Cr in the interlayer causes the formation of γ-Ni, Ni_3B, and Cr–boride phases. This fact shows that the Cr content in the interlayer affected the completion of isothermal solidification process. In a study, it has been shown that the Cr element could postpone the movement of B from the interlayer to the base metal [33].

Figure 6 depicts the microstructure of TLP joint specimens bonded at 1100 °C for 45 min via SEM. It can be seen that three main phases are distinguishable within the eutectic.

Solidification sequences occurring during transient liquid phase process for the GTD-111/BNi-9/In-718 could be investigated in accordance with the ternary diagram of Ni-B-Cr and also distribution coefficient of the elements and cooling the residual melt.

The principal controlling factor of the ISZ is the bonding time which will definitely affect the mechanical behavior of the bonding, too. The SEM images show that at 1100 °C/75 min, a totally eutectic-free ISZ containing no additional precipitates could be achieved (Fig. 7). Based on the fact that elements such as Cr, Al, Nb, and Ti were not detected in the interlayer while their borides were present in the ISZ, it can be concluded that the base metal is dissolved (Table 2). During the TLP process, due to the dissolution of elements of Nb and Fe from IN-718 and the elements of Al, Ti, and Co from the GTD-111 base metal into the melt, chemical changes occurred in this zone which are known as the melt-back phenomena [1, 34].

Greater amounts of Cr, Al, Ti, and Co in the GTD-111 side with lower amounts of Nb compared with the corresponding values in IN-718 side confirm the dissolution of the base metal. Yuan et al. [33] studied the time required for the dissolution of the base metal. They found that with an increase in the k

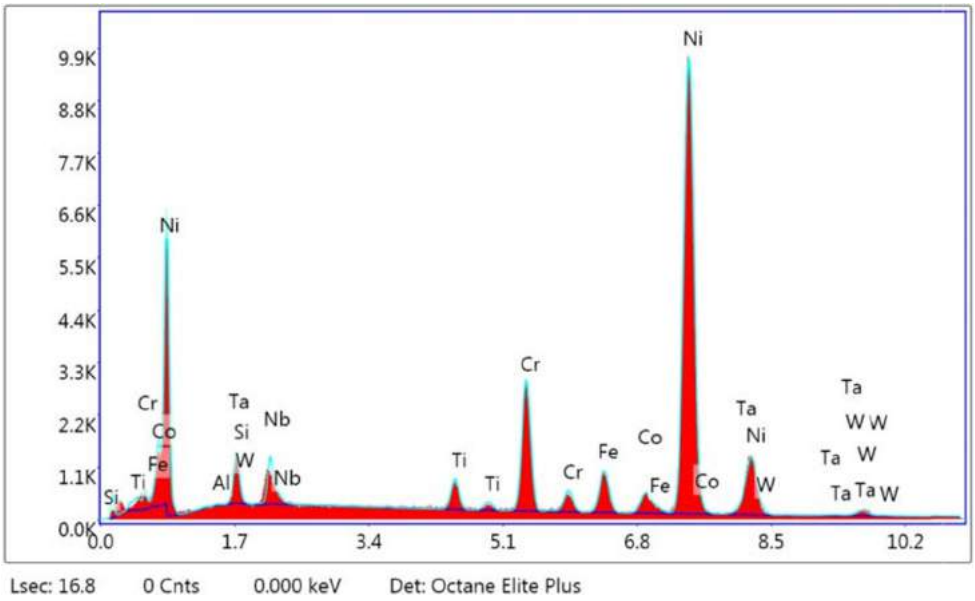

Fig. 5 EDS results of athermal solidification zone (ASZ)

coefficient, the dissolution of base metal will be completely decreased.

As it was mentioned, insufficient duration time triggers the emerging and remaining of the eutectic phase in the joint centerline. The formation of eutectic zone containing Ni-rich borides and γ solid solution which is confirmed by the EDS analysis is based on the Ni–B–Cr phase diagram. The first phase that is formed in the centerline of the joint at the cooling stage is the γ-Ni phase in the dendrite form that grows from the liquid/solid interface. During the creation of primary γ dendrites from the liquid-solid interface during cooling, elements with a segregation coefficient lower than unity such as Cr, Ti, and Mo would have the tendency to segregate into the remaining liquid while the dendrites are growing, hence decreasing the liquidus temperature [34].

Also, boron with a segregation coefficient of 8×10^{-3} in Ni–B hypoeutectic exhibits a strong tendency to segregate into the remaining liquid phase [35]. During solidification, the boride phases begin to form in between the dendrites by way of a eutectic reaction because of the increase in the concentration of the segregated elements in the liquid phase rather than their parallel solubility limit in austeniticγ. This results in the eutectic reaction from the remaining liquid, and the nickel-rich boride phase is formed during cooling: $L \rightarrow Ni\text{-rich boride} + \gamma$.

Solute element segregation is the first reason for the development of the solidification phase. The chemical composition changes by the alloy element in the base metal and interlayer are described by 3 stages:

- Stage I: solidification sequence in the ISZ: during this cycle, Ni-rich γ solid solution is formed from the remaining liquid.
- Stage II: the low distribution coefficient and low solubility of B in Ni (0.008 and 0.3 wt.% correspondingly,

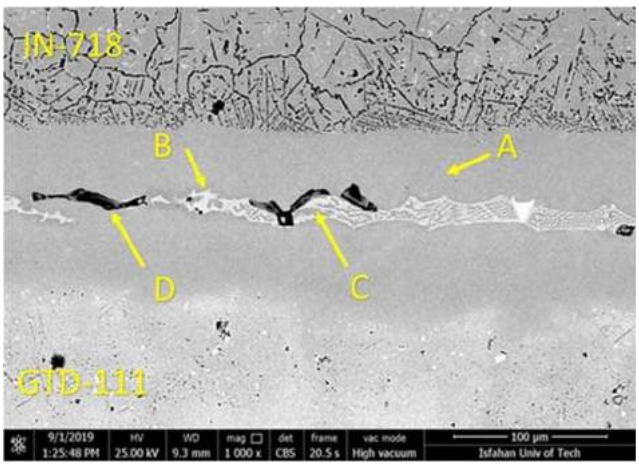

Fig. 6 SEM image of the ASZ. **a** γ-proeutectic. **b** Ni-rich boride. **c** γ-eutectic. **d** Cr-rich boride

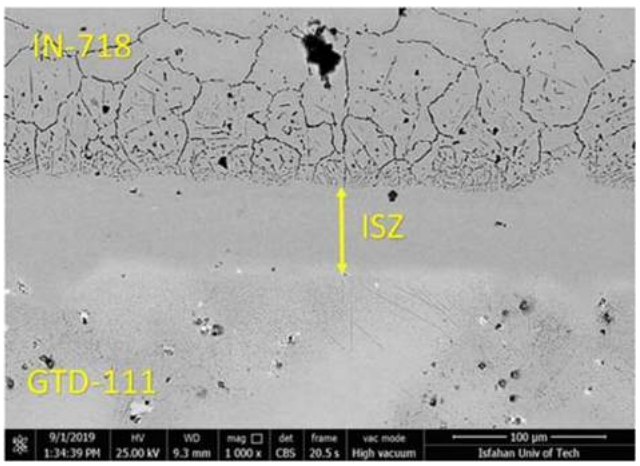

Fig. 7 SEM shows a totally eutectic-free ISZ at 1100 °C/75 min

according to the Ni-B binary phase diagram [35], lead to the rejection of B into the adjacent melt ending up with a liquid composition enrichment to the point where the primary solidification path crosses the eutectic line where the γ and Ni_3B phases are separated. After that, as the nickel boride and γ solid solution are concurrently formed by a eutectic reaction ($L \rightarrow Ni_3B + \gamma$), the solidification path follows the eutectic line. Due to high interfacial energy between the γ solid solution and nickel borides, a great driving force is needed for mutual nucleation of both phases during the melt phase transformation into normal eutectic structure [1]. In this investigation, based on microstructural study and EDS results, there was no silicide phase. It appears that the controlling factor for microstructural development in the ASZ is the boron content.

As shown in Fig. 8, due to the low solubility of the Cr element in Ni-boride and γ solid solution (10.11 at.% and 18 at.%, respectively), formation of the γ-eutectic and the Ni-rich boride solidification phases under the binary eutectic reaction along the e8 path brings about the Cr enrichment in the molten liquid [25].

The principal solidification direction is from the base metal towards the centerline joint. According to Tung et al. [36], in cooling conditions, firstly, the primary solidification phase, namely, Ni-rich γ phase, is formed. This phase enriches the remaining melt with B and Cr. As the cooling process continues, the binary eutectic of γ nickel and nickel borides will be solidified; therefore, the melt is enriched with chromium. Moreover, further cooling leads to binary eutectic of γ chromium and chromium borides.

As shown in Fig. 8, the Cr enrichment such as a decrement in temperature addresses the solidification path towards the E3 point. Then, the remaining liquid through ternary eutectic reaction at 1100 °C transforms into Ni-rich boride, Cr-rich boride, and eutectic γ solidification phase ($L \rightarrow \gamma + Ni_3B + CrB + \gamma$eutectic).

The EDS compositional analysis is shown in Fig. 9a, b. The results suggest that the formed phases in the ASZ are nickel-based solid solution phase and Ni-rich (Fig. 9a) and Cr-rich boride (Fig. 9b) phase. Moreover, other studies have reported similar eutectic microstructure in the centerline of TLP-bonded nickel-based superalloys. As an example, based on Johnson studies [24], if the level of boron is restricted, the ternary eutectic is not formed. Insufficient volume fraction of borides leads to the increase of other element content in the remaining liquid phase over the solid solubility limit in the nickel-phase solid solution. Hence, in the cooling stage, just two phases such as solid solution and nickel boride are formed in the ASZ. The TLP bonding of stainless steel 316L to Ti-6Al-4V using a Cu/Ni interlayer was proposed by Surendar et al. [37]. They reported that in high temperatures, the growth of eutectic microstructure is caused by melted phase shrinkage at the interface during non-isothermal solidification.

As can be seen in Figs. 5 and 6, the A–D marks show the primary γ, Ni-rich boride, eutectic γ, and Cr-rich boride. Although EDS has limitations in qualifying light elements, boron was identified in the EDS spectrum. Idowu et al. reported the formation of similar phases in the center of TLP-bonded joint of cast Inconel 738LC superalloy with an Ni–B–Cr interlayer [31]. Ohsasa et al. [24] studied the

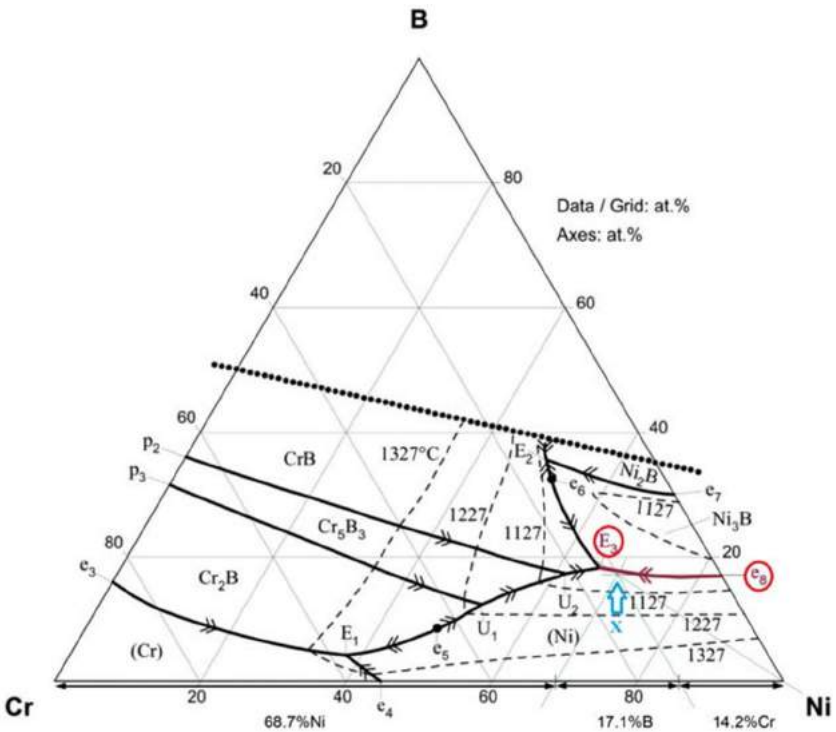

Fig. 8 Ternary phase diagram of Ni-B-Cr

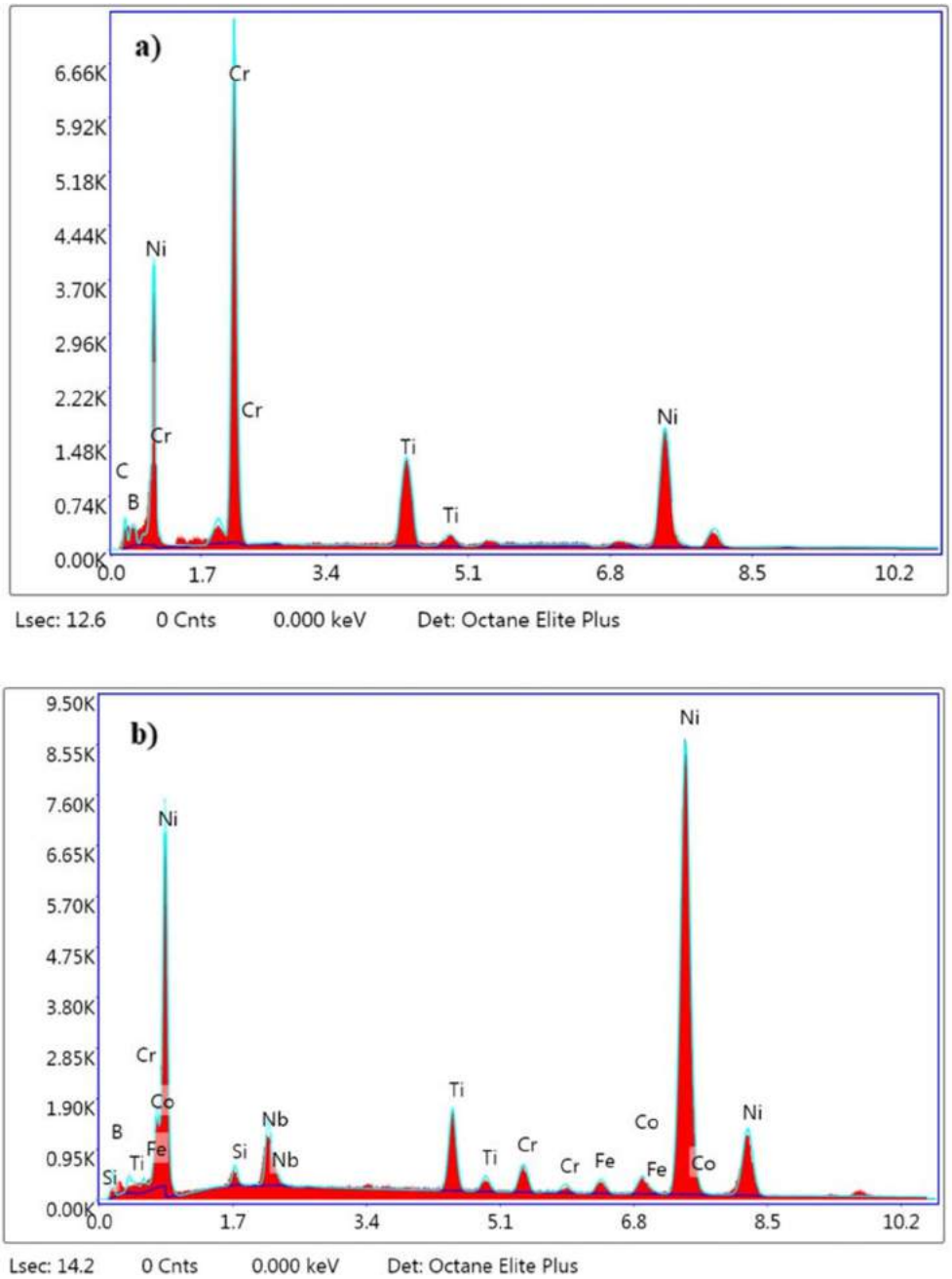

Fig. 9 SEM-EDS spectrum. **a** Cr–boride. **b** Ni–boride phases

solidification procedure of remaining liquid during the TLP bonding of pure nickel using the Ni–B–Cr interlayer by applying the Scheil simulation.

Their results indicated the formation of a ternary eutectic at the TLP centerline composed of Ni-based γ solid solution, Ni borides (Ni_3B), and Cr boride (CrB) solid solution at 997 °C. They reported that for the samples with the initial temperature of 1100 °C, solidification of the residual liquid formed γ phase in the first place. Subsequently, the eutectic reaction $L \rightarrow \gamma + Ni_3B$ occurred at 1042–1100 °C. The solidification process was reported to be completed at 997 °C with a ternary eutectic reaction $L \rightarrow \gamma + Ni_3B + CrB + \gamma eutectic$. Micro-hardness measurement results are indicative of extremely high hardness even almost equal to the base metal value.

Boron diffusion from the bonding zone into the base metal indicates that boron can decrease the carbon solubility in

nickel alloy and also justifies the existence of carboboride phases containing Co, Ni, Cr, and Nb elements as a high trigger for boride formation. Also, secondary phase formation induces Cr-rich carboborides. Idowu et al. found Cr, W, and Mo carboborides in the nickel-based IN738LC superalloy joint interface, implying the Ni–Cr–B interlayer at 1130 °C [31].

3.5 Diffusion affected zone

In the isothermal solidification zone and athermal solidification zone, the main solidification phenomena are the liquid phase solidification and liquid diffusion carried out in the aforementioned zone but the main solidification phenomena in the diffusion affected zone or DAZ include the solid state precipitation and solid-state diffusion. With the transfer from the joint region close to the base metals, the boride compound concentration is reduced. It was shown that the boride combinations locked parent metal grains in the DAZ of IN-718 alloy and more grain boundaries existed near the joint. As can be seen in Figs. 10 and 11, the morphology of the secondary phase particles observed at the DAZ of GTD-111 consists of blocky and needle-shaped Cr-rich boride (secondary) precipitates. The secondary precipitates were formed in the γ-matrix close to the interface of the joint/base metal. A morphological assessment of the precipitates brings up the clue that they were not formed during the cooling and solidification process but were formed during the bonding process itself. Gale and Wallach [38] concluded from their metallographic studies that in spite of the grain growth in the base metal, after the bonding process, the size of grains did not change in the DAZ. It is obvious that the grains' growth could be carried on throughout the isothermal holding while it does not occur during the cooling process. Gale and Wallach reported the same result in their study [38]. Hence, it could be concluded that the particles are formed during the grain growth at bonding temperature, sticking to the grain boundaries.

Figure 10 a and b show the different grains and grain boundaries of IN718 after the bonding temperature. Figure 10 a depicts the image of secondary electrons and Fig. 10 b shows the image of backscatter electrons. The chemical composition of blocky and needle-shaped precipitates is shown in Table 3. EDS compositional analysis of metallic elements suggested that precipitates are Cr-rich boride. Ni and Cr were detected in both types of precipitates by EDS analysis. The spot analysis of needle-shaped precipitates disclosed that, as expected, this zone was rich in Cr, B, Ni, and C which confirms the presence of Cr-rich boride precipitates.

The development of secondary precipitates in the DAZ involves two steps: step I: the transfer of boron atoms close to the base metal to wherever there are strong boride-forming elements like Cr, W, and Ta; step II: boron diffusion into the base metal close to the ISZ/base metal interface. After exceeding the solubility limit of boron in the base metal, boride precipitation happens in the γ matrix. The presence of strong boride-forming elements such as Cr, Mo, Nb, Ta, and W could cause the creation of precipitates in the DAZ. There are two possible mechanisms for the formation of these borides. Mechanism one is the solid-state diffusion of boron into the base metal prior to complete dissolution [38]. Mechanism two is the solid-state diffusion of boron into the base metal throughout the isothermal solidification [39].

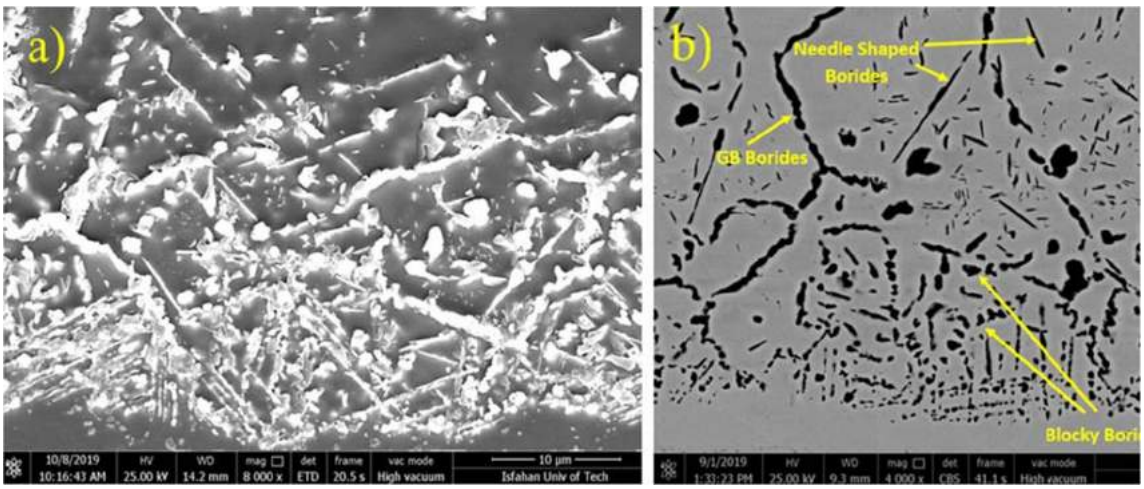

Fig. 10 Microstructure of diffusion affected zones in IN718 contains grain boundaries and grains consist of needle-shaped and blocky borides. **a** Secondary electron picture. **b** Backscatter electron picture

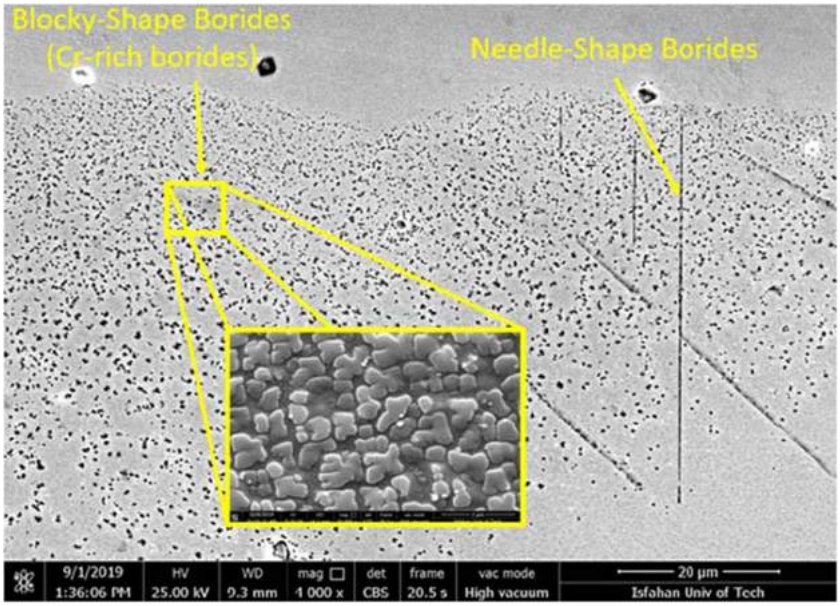

Fig. 11 Morphology of the secondary phase particles observed at diffusion affected zone of GTD-111 consists of blocky and needle-shaped particles. **a** Blocky. **b** Blocky and needle-shaped particles

Chromium, niobium, tantalum, and wolfram borides settling in the DAZ result in incremented chromium and molybdenum content surrounding the boride precipitates and reduce local corrosion resistance of the matrix. However, the aging behavior of IN-718 superalloy is highly dependent on the niobium content. Hence, niobium boride formation in the DAZ, depleting the adjacent matrix from niobium, could affect the aging behavior of this region [40]. Moreover, in the case of GTD-111, significant amounts of chromium, cobalt, and titanium borides are anticipated in the DAZ.

4 Bonding time effect on the joint microstructure

Joint microstructure is highly dependent on the bonding time which is subject to the existence of interdiffusion between the base metals and the interlayer. Figure 12 depicts the joint microstructure after different (45, 60, and 75 min) bonding times. By considering 5 measurements, we can estimate the width of the ASZ, ISZ, and bonding zone. The sequences of the eutectic structure vanishing due to the isothermal solidification completion and the width of the ASZ, ISZ, and bonding zone are illustrated in Fig. 13.

It can be seen that the joint width increases with the decrease of isothermal solidification rate at the bonding temperature of 1100 °C in the bonding time of 45 min and decreases with the increase of isothermal solidification rate in the bonding time of 75 min. This is based on two factors: (I) boron flux decreasing to the base metal at the bonding temperature of 1100 °C due to the absence of boride precipitates in the base metal; (II) enhancement of the remaining liquid with some base metal alloying elements throughout isothermal solidification and dissolution. The bonding time not only affects the joint width but also influences the ASZ and ISZ width. Of course, there is an inverse correlation between the ASZ and ISZ width against the bonding zone. The ASZ width is another factor which is affected by the bonding time and is in reverse proportion with the bonding time. In the case of increasing the bonding time, the completion of isothermal

Table 3 Chemical composition of DAZ particles (wt%), blocky and needle-shaped precipitates

Particles	**Ni**	**Cr**	**Co**	**Ti**	**Al**	**Mo**	**Ta**
Blocky precipitates (for GTD-111)	22.07	47.61	8.80	4.15	1.64	4.08	3.17
Needle-shaped precipitates (for GTD-111)	11.92	60.34	9.22	5.50	2.20	2.00	5.02
Particles	**Ni**	**Cr**	**Si**	**Ti**	**Fe**	**Mo**	**Nb**
Blocky precipitates (for IN-718)	19.12	46.29	1.15	1.09	13.58	9.05	9.72
Needle-shaped precipitates (for IN-718)	17.96	48.58	0.31	1.90	20.35	0.34	6.43

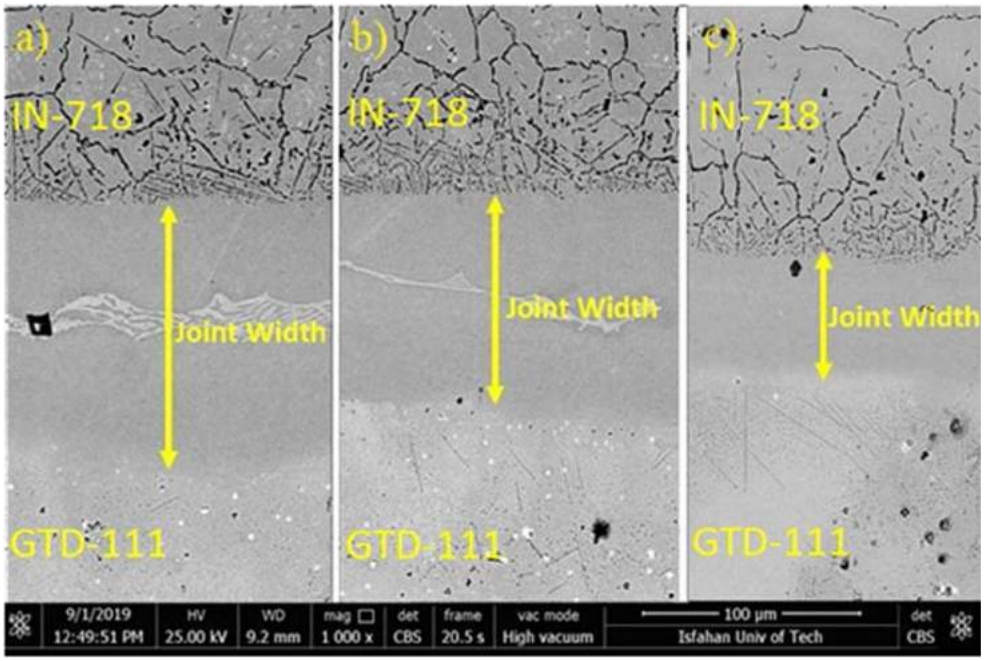

Fig. 12 SEM graph from the joint region contains bonding times **a** 45 min, **b** 60 min, and **c** 75 min

solidification occurred at the bonding time of 75 min and the amount of eutectic structure decreased. Boron concentration of the interlayer that affects the joint width was reported by reference [41].

5 Effect of isothermal solidification on mechanical properties

5.1 Micro-hardness test

Measuring the micro-hardness of the bonding is one of the factors which could be used to determine the bonding mechanical properties. The assessment of secondary precipitates could help predicting the microstructure. Figure 14 illustrates the micro-hardness profile of the specimen at the bonding zone with respect to the bonding time at 1100 °C. The micro-hardness is increasing from the base metal area towards the bonding zone, significantly at the DAZ in which intermetallic compounds and boride precipitates existed. Maximum micro-hardness was seen at the DAZ on the GTD-111 side at 1100 °C/1 min while micro-hardness is significantly low at the ISZ. Farzadi et al. reported that the highest hardness occurs in the DAZ near the interface [42]. Micro-hardness between the base metal and joint region depends on the precipitation hardening mechanisms and interdiffusion of the alloy elements. In the GTD-111 side, insufficient diffusion of solid solution strengthening alloying elements for example Cr, Co, Nb, Al, Ti, and Ta results in reduced hardness of the ISZ. The micro-hardness profile of the isothermal bonding

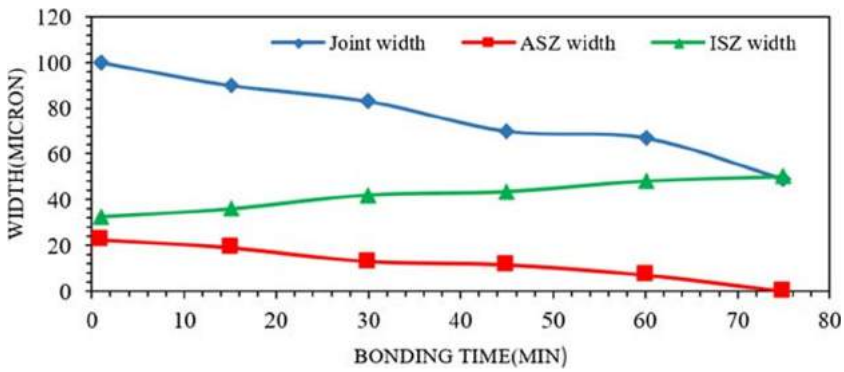

Fig. 13 Width of the ASZ, ISZ, and bonding zone in the different bonding times

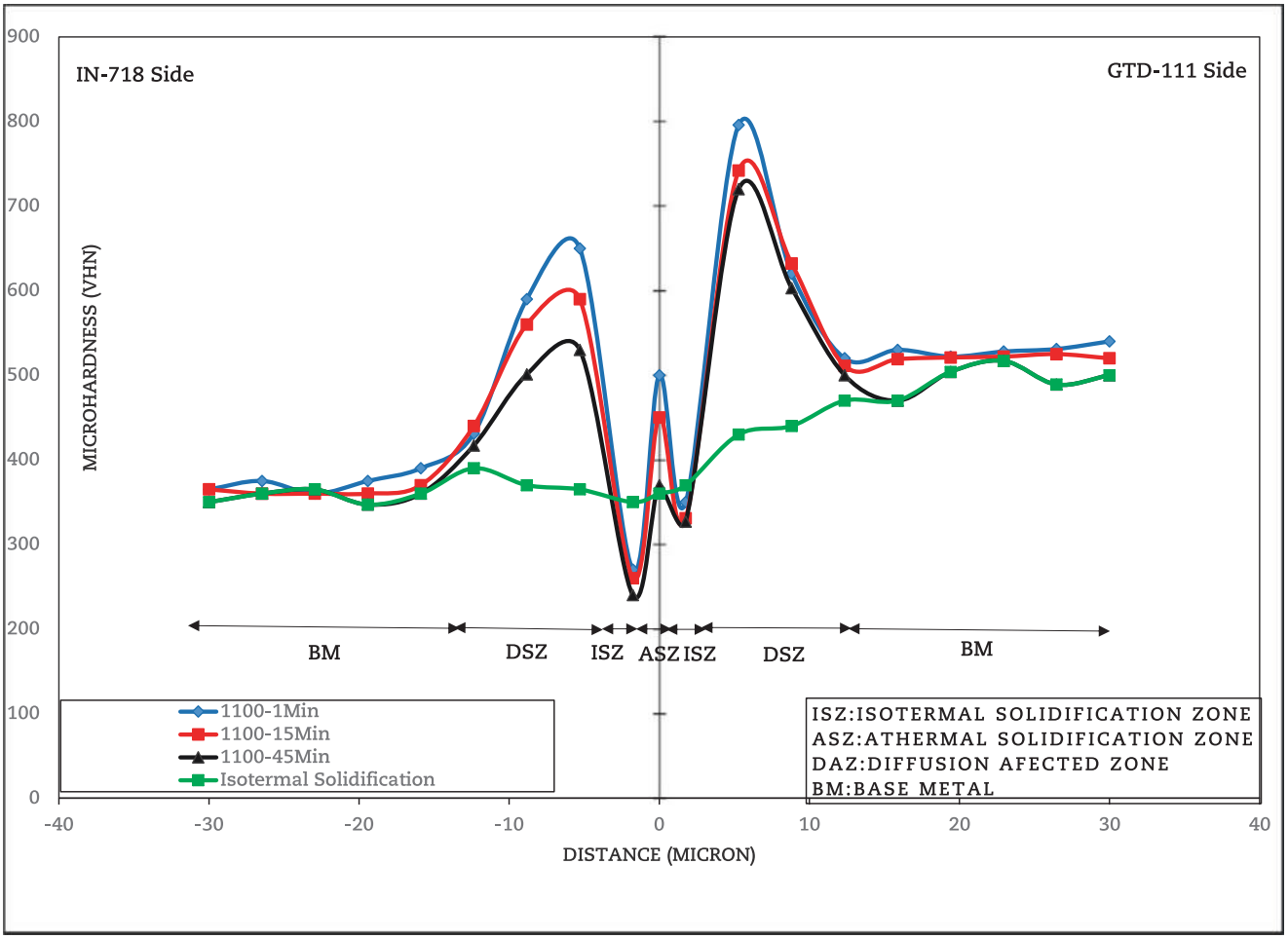

Fig. 14 Micro-hardness profile of the TLP-bonded samples at 1100 °*C* for different bonding times

zone is free of any brittle or hard intermetallic phases which are depicted in Fig. 14. Furthermore, the minimum hardness in the joint area belongs to the ISZ. The nature of Ni-rich γ solid solution is a soft phase. At the bonding zone, the highest micro-hardness area is observed at the ASZ due to the existence of boride compounds such as brittle and hard nickel and chromium borides. High micro-hardness of the eutectic compounds is originated from the formation of a coherent boride matrix such as nickel or chromium boride that brings up a metallurgical notch which leads to decreased capacity of the joint load endurance [43]. A relation between the bonding time and mechanical properties, i.e., micro-hardness, is justified by the type of interdiffusional elements within the base metal and the bonding zone. After completion of isothermal solidification, the average micro-hardness of the ISZ was observed with an increment from 220 to 315 in the bonding time of 45 to 75 min.

5.2 Shear strength

Bonding shear strength accelerates with the decrease of micro-hardness. Thus, it could be noted that prior to the completion of isothermal solidification, eutectic zone is the dominant factor for the decreased bonding shear strength. Figure 15 shows the shear strength vs. bonding time results of the TLP bonding at 1100 °C for 1–75 min of bonding time obtained from the shear strength test. So, with the increasing bonding time from 1 to 75 min, the joint shear strength increased. It can be seen that the shear strength is in a reverse proportion with the ASZ width. In other words, increasing the width size of the ISZ and decreasing of the boride compounds in these areas result in increasing the shear strength. For the specimen which was bonded for 30 min, the bonding zone consists of eutectic phases or compounds at the bonding centerline zone. In other words, it is called the incomplete isothermal bonding zone. By increasing the bonding time to 60 and 75 min, the intermetallic compounds disappeared where isothermal solidification was completed. According to the results, the specimen with complete isothermal solidification zone (bonding time = 75 min) has greater shear strength and therefore higher ductility and energy absorption compared with the specimens with incomplete solidification zones (bonding time < 75 min) which contain brittle intermetallic

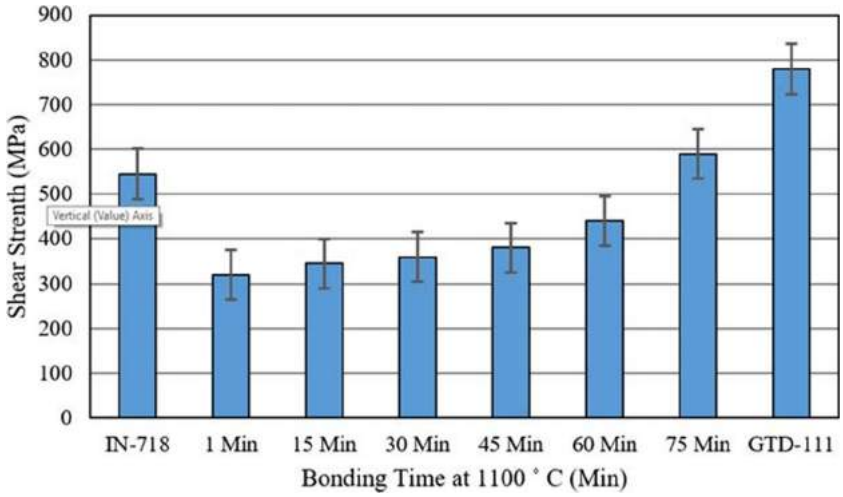

Fig. 15 Shear strength of the joints for different bonding times

compounds at their bonding centerlines. During the loading, the brittle and hard structure generates a low-resistant path for crack propagation.

Figure 16 illustrates the shear strength of various specimens versus the bonding time. This figure proves that the ASZ size to ISZ size ratio affects the shear strength and triggers metallurgical notch. Constant shear strength is inspected when this ratio is greater than 0.5, while at ratios lower than 0.4, the shear strength which is a eutectic depressant factor would increase. Therefore, when isothermal solidification is still incomplete, the eutectic microstructure amount is the controlling factor for the bonding strength [40].

Figure 17 shows SEM micrographs of the fractured specimen cross section and fracture surface of the bonded sample at 1100 °C for 15, 30, and 75 min. The selected sample includes the ASZ and ISZ areas. The specimen with the bonding time of 15 min shows a cleavage fracture surface which proves a brittle fracture. Because of brittle intermetallic compounds in the joint region, this mode of fracture is obtained. Based on the fracture image, failure happened due to the existence of inter-

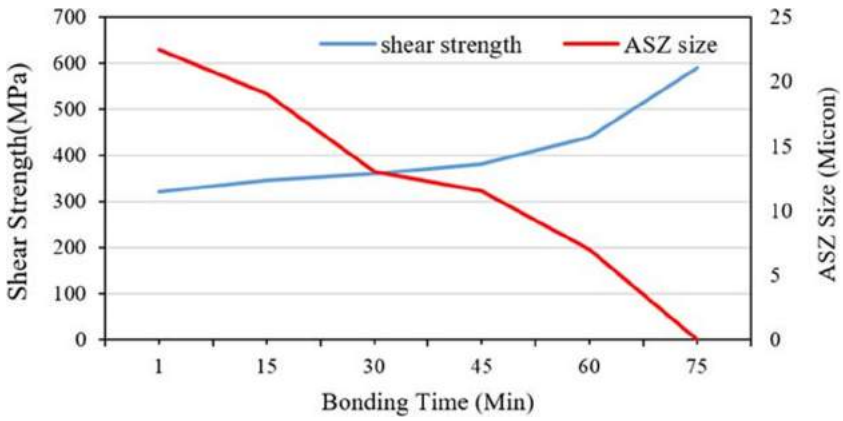

Fig. 16 The shear strength is in reverse proportion with the ASZ width

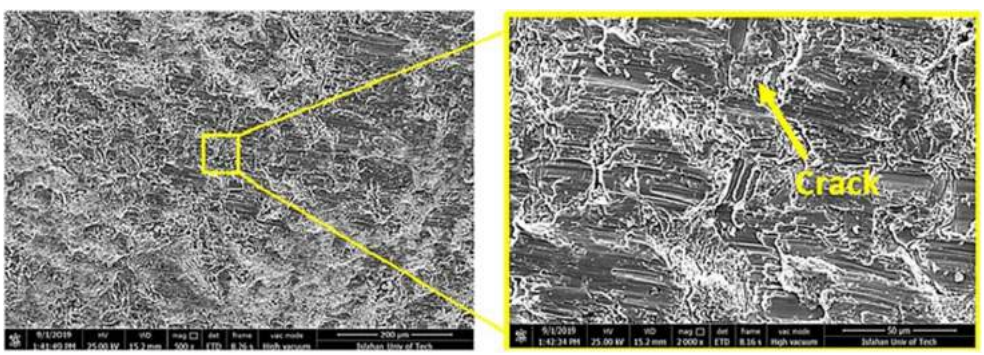

Fig. 17 SEM images of the fracture surface of shear test of TLP joint samples carried out at 1100 °C for bonding times of **a** 15 and **b** 30 min

metallic compounds in the central joint region. Therefore, preferential position to crack created by the borides layer with indigent plastic deformation resistance leads to the low tensile-shear strength. Ojo et al. reported that one of the preferential low-resistance paths for crack propagation is the zone containing continuous borides [11].

6 Conclusion

Dissimilar TLP bonding of GTD-111 and IN-718 nickel–based superalloys was carried out at different bonding times using a Ni–Cr–B interlayer (BNi-9). The microstructure and mechanical properties of the bonded specimens were investigated. The following results could be driven from the current study:

1 Borides of Cr and Ni were observed as the eutectic structure for the joints made at 1100 °C in 15 min. The DAZ in half of IN718 contained Nb and Cr and the DAZ in half of GTD-111 contained Ta, Ti, and Cr borides. In the case of increasing the bonding times at a constant temperature (1100 °C), the size of eutectic phases decreased at the joint centerline and the ISZ became wider.
2 The DAZ contained Cr-rich boride particles with needle-shaped and blocky precipitates, which appeared from the solid-state diffusion of boron element into the adjoining base metal.
3 Completion of isothermal solidification and disappearance of eutectic structure were accomplished at 1100 °C for 75 min.
4 The solidification sequence of the residual liquid in the joint centerline was found to be (1) α Ni-solid solution, (2) formation of an α eutectic phase and a (Ni,Cr)3B eutectic phase, and (3) solidification of Cr-rich alloys such as BNi-9 ends with the reaction L ➔ α + (Ni,Cr)3B + CrB.
5 The hardness profiles of the bonding zone revealed that the highest micro-hardness area is observed at the ASZ which is due to the existence of boride compounds such as brittle and hard nickel and chromium borides. High micro-hardness of the eutectic compounds is originated from the formation of a coherent boride matrix such as nickel or chromium boride that brings up a metallurgical notch which leads to the decreased capacity of the joint load endurance.

References

1. Pouranvari M, Ekrami A, Kokabi A (2008) Microstructure development during transient liquid phase bonding of GTD-111 nickel-based superalloy. J Alloys Compd 461(1–2):641–647
2. Shamsabadi AY, Bakhtiari R (2016) TLP bonding of IN738/MBF20/IN718 system. J Alloys Compd 685:896–904
3. Ojo OA (2004) On liquation cracking of cast Inconel 738LC superalloy welds. Ph.D. Dissertation, University of Manitoba, Canada
4. Yan P, Wallach E (1993) Diffusion-bonding of TiAl. Intermetallics 1(2):83–97
5. Campbell CE, Boettinger WJ, Kattner UR (2002) Development of a diffusion mobility database for Ni-base superalloys. Acta Mater 50(4):775–792
6. Hattori T, Sakai S, Sakamoto A, Fujiwara C (1994) Brazeability of aluminum in vacuum-nitrogen partial-pressure atmosphere brazing. Weld J Incl Weld Res Suppl 73(10):233s
7. Tung S, Lim L, Lai M, Wu H (1997) Evolution of nickel borides in Ni-Si-B brazed joints of nickel during post-braze heat treatment. Mater Sci Technol 13(12):1051–1056
8. Rabinkin A (2004) Brazing with (NiCoCr)–B–Si amorphous brazing filler metals: alloys, processing, joint structure, properties, applications. Sci Technol Weld Join 9(3):181–199
9. Jin T, Li W, Sun X-F, Guan H-R, Hu Z-Q (2008) Creep fracture mechanism of TLP joint of a Ni-base single crystal superalloy. J Alloys Compd 457(1–2):185–190
10. Qian M, Lippold J (2003) The effect of annealing twin-generated special grain boundaries on HAZ liquation cracking of nickel-base superalloys. Acta Mater 51(12):3351–3361
11. Ojo O, Richards N, Charturvedi M (2004) Effect of gap size and process parameters on diffusion brazing of Inconel 738. Sci Technol Weld Join 9(3):209–220
12. Ahn Y, Yoon B, Kim H, Lee C (2002) Effect of dilution on the behavior of solidification cracking in PTAW overlay deposit on Ni-Base superalloys. Met Mater Int 8(5):469–477
13. Ye X, Hua X, Wang M, Lou S (2015) Controlling hot cracking in Ni-based Inconel-718 superalloy cast sheets during tungsten inert gas welding. J Mater Process Technol 222:381–390
14. Duvall D, Owczarski W, Paulonis D (1974) TLP bonding: a new method for joining heat resistant alloys. Weld J(NY) 53(4):203–214
15. Ekrami A, Khan T (1999) Transient liquid phase diffusion bonding of oxide dispersion strengthened nickel alloy MA758. Mater Sci Technol 15(8):946–950
16. Ekrami A, Khan T, Malik H (2003) Effect of transient liquid phase diffusion bonding on properties of ODS nickel alloy MA758. Mater Sci Technol 19(1):132–136
17. Bakhtiari R, Shamsabadi AY, Moradi KA (2020) Shear strength/microstructure relationship for dissimilar IN738/IN718 TLP joints. Weld World 64(1):219–231
18. MacDonald W, Eagar T (1992) Transient liquid phase bonding. Annu Rev Mater Sci 22(1):23–46
19. Tuah-Poku I, Dollar M, Massalski T (1988) A study of the transient liquid phase bonding process applied to a Ag/Cu/Ag sandwich joint. Metall Trans A 19(3):675–686
20. Paulonis D, Oblak J, Duvall D (1969) Precipitation in nickel-base alloy 718. Pratt and Whitney Aircraft, Middletown, Conn
21. Pouranvari M, Ekrami A, Kokabi A (2013) Solidification and solid state phenomena during TLP bonding of IN718 superalloy using Ni–Si–B ternary filler alloy. J Alloys Compd 563:143–149
22. Schilke P, Beltran A, Foster A, Pepe J (1996) Advanced Gas Turbine Materials and Coatings, 39th GE Turbine State-of-the-Art Technology Seminar. GE Power Systems, GER-3569F, 22
23. Amiri D, Sajjadi SA, Bakhtiari R, Kamyabi-Gol A (2018) The role of TLP process variables in improvement of microstructure and mechanical properties in TLP joints of GTD-111/Ni-Cr-Fe-B-Si/GTD-111 system. J Manuf Process 32:644–655
24. Ohsasa K, Narita T, Shinmura T (1999) Numerical modeling of the transient liquid phase bonding process of Ni using Ni-B-Cr ternary filler metal. J Ph Equilib 20(3):199–206
25. Bondar A, MSIT, B (2007) B-Cr-Ni (boron-chromium-nickel) nonferrous metal ternary systems. Selected soldering and brazing

systems: phase diagrams, crystallographic and thermodynamic data. Non-Ferrous Metal Systems. Part 3: Selected Soldering and Brazing Systems, pp 153–167
26. Siredey-Schwaller N, Hamel-Akré J, Peltier L, Hazotte A, Bocher P (2017) Solidification sequence of Ni-Si-Cr~ 3wt% B brazing alloys. Welding in the World 61(6):1253–1265
27. Danflou HL, Marty M, Walder A (1992) Formation of serrated grain boundaries and their effect on the mechanical properties in a P/M nickel base superalloy. Superalloys 1992:63–72
28. Hoffelner W, Kny L, Stickler R, McCall W (1979) Effects of aging treatments on the microstructure of the Ni-base superalloy IN-738. Mater Werkst 10(3):84–92
29. Daleo A, Wilson JR (1998) GTD111 alloy material study. J Eng Gas Turbines and Power 120:375–381
30. Sajjadi SA, Nategh S, Guthrie RI (2002) Study of microstructure and mechanical properties of high performance Ni-base superalloy GTD-111. Mater Sci Eng A 325(1–2):484–489
31. Idowu O, Ojo O, Chaturvedi M (2006) Microstructural study of transient liquid phase bonded cast INCONEL 738LC superalloy. Metall Mater Trans A 37(9):2787–2796
32. Cieslak M, Stephens J, Carr M (1988) A study of the weldability and weld related microstructure of Cabot alloy 214. Metall Trans A 19(3):657–667
33. Yuan X, Kim MB, Kang CY (2009) Characterization of transient-liquid-phase-bonded joints in a duplex stainless steel with a Ni–Cr–B insert alloy. Mater Charact 60(11):1289–1297
34. Sung P, Poirier DR (1999) Liquid-solid partition ratios in nickel-base alloys. Metall Mater Trans A 30(8):2173–2181
35. Massalski T, Okamoto H, Subramanian P, Kacprzak L (1986) Binary alloy phase diagrams, ASM, Metals Park. Ohio 1987:22
36. Tung S, Lim L, Lai M (1996) Solidification phenomena in nickel base brazes containing boron and silicon. Scr Mater 34(5):763–769
37. Surendar A, Lucas A, Abbas M, Rahim R, Salmani M (2019) Transient liquid phase bonding of stainless steel 316 L to Ti-6Al-4 V using Cu/Ni multiinterlayer: microstructure, mechanical properties, and fractography. Weld World 63(4):1025–1032
38. Gale W, Wallach E (1991) Microstructural development in transient liquid-phase bonding. Metall Trans A 22(10):2451–2457
39. Pouranvari M, Ekrami A, Kokabi A (2009) Effect of bonding temperature on microstructure development during TLP bonding of a nickel base superalloy. J Alloys Compd 469(1–2):270–275
40. Pouranvari M, Ekrami A, Kokabi A (2013) TLP bonding of cast IN718 nickel based superalloy: process–microstructure–strength characteristics. Mater Sci Eng A 568:76–82
41. Pouranvari M (2015) Solid solution strengthening of transient liquid phase bonded nickel based superalloy. Mater Sci Technol 31(14):1773–1780
42. Farzadi A, Esmaeili H, Mirsalehi S (2019) Transient liquid phase bonding of Inconel 617 superalloy: effect of filler metal type and bonding time. Weld World 63(1):191–200
43. Pouranvari M, Ekrami A, Kokabi A (2008) Microstructure–properties relationship of TLP-bonded GTD-111 nickel-base superalloy. Mater Sci Eng A 490(1–2):229–234